Successes and failures of the k·p method: A direct assessment for GaAs/AlAs quantum structures

D. M. Wood* and Alex Zunger
National Renewable Energy Laboratory, Golden, Colorado 80401
(Received 27 October 1995)

The **k·p** method combined with the envelope-function approximation is the tool most commonly used to predict electronic properties of semiconductor quantum wells and superlattices. We test this approach by comparing band energies, dispersion, and wave functions for GaAs/AlAs superlattices and quantum wells as computed directly from a pseudopotential band structure and using eight-band **k·p**. To assure equivalent inputs, all parameters needed for the **k·p** treatment are extracted from calculated bulk GaAs and AlAs pseudopotential band structures. Except for large exchange splittings in the in-plane dispersion for thin superlattices, present in pseudopotential calculations but absent from the **k·p** results, we find generally good agreement for heterostructure hole bands within ~200 meV of the GaAs valence-band maximum. There are systematic errors in band energies and dispersion for deeper hole bands (all other than hh1 and lh1) and significant qualitative and quantitative errors for the conduction bands. Errors for heterostructure conduction states which are derived from the zinc-blende Γ point diminish as length scales increase beyond ~20 ML, while significant errors persist for *L*- and *X*-derived states. For *bulk* GaAs and AlAs, eight-band **k·p** bands agree well with pseudopotential results very near the zinc-blende Γ point (where **k·p** parameters are fit) but the first GaAs *X* point conduction band is ≃26 eV too high with respect to the pseudopotential result. We show that this inadequate description of the *bulk* band dispersion is the principal source of **k·p** errors in these *heterostructures*. A wave-function projection analysis shows that **k·p** errors for heterostructures simply reflect corresponding errors for the bulk constituents, weighted by the amount that such bulk states participate in heterostructure states.

I. INTRODUCTION

Optoelectronic applications[1] often exploit electronic properties of artificial heterostructures, such as superlattices and quantum wells, with characteristic dimensions of 100 Å. Their electronic properties could, in principle, be interpreted using the same tool applied successfully to bulk solids, namely, a complete band structure. Nanostructure single-particle energies and wave functions would then be solutions to

$$\left[\frac{\hat{\mathbf{p}}^2}{2m_0}+V(\mathbf{r})\right]\psi(\mathbf{r})=\varepsilon\psi(\mathbf{r}), \tag{1}$$

where $V(\mathbf{r})$ is the total three-dimensional *atomistic* potential, including all effects of the interfaces between materials A and B for the A/B heterostructures. $V(\mathbf{r})$ could be computed self-consistently from the occupied states using, e.g., density functional theory, or it could be approximated as a superposition of screened atomic potentials,[2,3] i.e.,

$$V(\mathbf{r})=\sum_{i,\mathbf{R}} v_i(\mathbf{r}-\mathbf{R}-\mathbf{d}_i) \tag{2}$$

for atom species i at basis site $\mathbf{d}_i$ in cell $\mathbf{R}$. If $V(\mathbf{r})$ is periodic,[4] the wave function is of Bloch form

$$\psi_{n\mathbf{k}}(\mathbf{r})\equiv\exp[i(\mathbf{k}\cdot\mathbf{r})]u_{n\mathbf{k}}(\mathbf{r}), \tag{3}$$

with $\varepsilon=\varepsilon_n(\mathbf{k})$. To solve Eq. (1), the wave function is generally expanded in a set of variationally complete basis functions, e.g., plane waves:

$$\psi_{n\mathbf{k}}(\mathbf{r})=\exp[i(\mathbf{k}\cdot\mathbf{r})]\sum_{|\mathbf{G}|<G_{\max}} c_{n,\mathbf{k}}(\mathbf{G})\exp[i(\mathbf{G}\cdot\mathbf{r})]. \tag{4}$$

One computes matrix elements of $V(\mathbf{r})$ in this basis, and diagonalizes Eq. (1) using iterative minimization[5] or techniques linear in[3] the atom number. The cutoff parameter $G_{\max}$ is varied to achieve practical convergence of $\varepsilon_n(\mathbf{k})$.

Because of the very large number of monolayers spanning ~100 Å nanostructures, they have until very recently[3] been beyond the reach of such *direct* electronic structure calculations [Eqs. (1)–(4) above], the conventional computational effort for which scales as the cube of the number of atoms. The spectroscopy of nanostructures is instead interpreted[6] using an approach so common that we term it the ''standard model'': the **k·p** method together with the envelope-function approximation (EFA). The **k·p** approach[7,8] uses a perturbation theory description of band dispersion for pure A or B within a small set of near-edge bands identified as physically relevant. In the EFA, the form used for the wave function in the heterostructure assumes that envelope functions vary on a scale much larger than the lattice constant of either A or B. The sole remnant of the atomistic $V(\mathbf{r})$ is an abrupt jump in material properties at the A/B interface. The **k·p**+EFA combination can be an extremely concise representation of heterostructure electronic properties, usually requiring only material parameters for the pure bulk materials A and B and dimensions and orientations of the A and B regions. In particular, the computational effort is essentially independent of the number of atoms in the system.

Although it has been eminently successful in a variety of applications,[9,10] often overlooked formal restrictions on the

standard model, compromise its description of an A/B heterostructure. The fact that its parameters are usually fit to experimental data has also made it difficult to appraise these limitations. In contrast to the direct approach of Eqs. (1)–(4), the standard model (a) omits discrete crystal symmetries, e.g., point-group symmetry differences between an odd and even number of layers in A_nB_m superlattices[11] or thin films;[12] (b) usually assumes a constant potential in each region and neglects the spatial dependence of wave functions transverse to the heterostructure modulation direction; (c) attempts to describe nanostructure wave functions in terms of a few Bloch states, neglecting their differences in materials A and B; and (d) can describe band dispersion only in an (unspecified) region near the heterostructure zone center.

Other methods have been applied to heterostructures, e.g., the tight-binding approach.[13] Although it preserves an atomistic description, like the $\mathbf{k}\cdot\mathbf{p}$ approach it suffers from a variationally limited, very small set of basis functions and a microscopically undefined potential. Furthermore, previous comparisons of the standard model with the tight-binding method[13,14] have generally suffered from the fact that material parameters were drawn from different sources. For moderate m and n, A_nB_m superlattices and A_n/B quantum wells provide a convenient opportunity to test the standard model against the direct approach, *provided* the parameters required by the former are calculated from the latter. Using AlAs-GaAs heterostructures as examples, in this paper we contrast $\mathbf{k}\cdot\mathbf{p}$+EFA and direct diagonalization [Eqs. (1)–(4)] for trends in (i) band energies, (ii) wave function amplitudes, and (iii) band dispersion.

II. THE k·p+EFA "STANDARD MODEL"

A. Representing bands of bulk materials

For pure bulk crystals, the cell-periodic part $u_{n\mathbf{k}}(\mathbf{r})$ [Eq. (3)] of the Bloch function in Eq. (1) obeys the equation

$$\left[\frac{\hat{\mathbf{p}}^2}{2m_0}+V(\mathbf{r})+\frac{\hbar}{m_0}\mathbf{k}\cdot\hat{\mathbf{p}}+\frac{\hbar^2k^2}{2m_0}\right]u_{n\mathbf{k}}(\mathbf{r})=\varepsilon_n(\mathbf{k})\,u_{n\mathbf{k}}(\mathbf{r}). \tag{5}$$

Since the states $\{u_{n\mathbf{k}_0}(\mathbf{r})\}$ at $\mathbf{k}\equiv\mathbf{k}_0$ form a complete set for any function periodic in the lattice,[15] we may use them as a basis for $u_{n\mathbf{k}}(\mathbf{r})$:

$$u_{n\mathbf{k}}(\mathbf{r})=\sum_{n'}^{N} b_{n'}u_{n'\mathbf{k}_0}(\mathbf{r}), \tag{6}$$

where N is the number of such states used. Inserting into Eq. (5), we find[7,8] the matrix equation,

$$\sum_{n'}^{N}\left\{\left[\varepsilon_n(\mathbf{k}_0)-\varepsilon_n(\mathbf{k})+\frac{\hbar^2}{2m_0}(k^2-k_0^2)\right]\delta_{n,n'}+\frac{\hbar}{m_0}(\mathbf{k}-\mathbf{k}_0)\cdot\mathbf{p}_{n,n'}\right\}b_{n'}=0. \tag{7}$$

The effects of $V(\mathbf{r})$ are now encoded in the momentum (dipole) matrix elements

$$\mathbf{p}_{n,n'}\equiv\langle u_{n\mathbf{k}_0}|\hat{\mathbf{p}}|u_{n'\mathbf{k}_0}\rangle. \tag{8}$$

Nonparabolic dispersion of band n is thus entirely due to states n' to which it is coupled by dipole matrix elements at $\mathbf{k}_0$. Although Eq. (7) includes terms only through second order in $\mathbf{k}$, if diagonalized using a sufficiently large number N of zone-center Bloch states $\{u_{n\mathbf{k}_0}(\mathbf{r})\}$, it would exactly predict the *full* (nonparabolic) band dispersion throughout the Brillouin zone. Thus, Eq. (7) is equivalent to solving Eq. (1), provided each uses a converged basis. We term this, in principle, exact parametrization of the full band structure of Eq. (7) the "$\mathbf{k}_0$ representation." Conventional approximations for semiconductors[7,8] use $\mathbf{k}_0=0\equiv\Gamma$, but make two simplifying *assumptions*.

(1) *Truncation/degenerate perturbation theory:* The set of zone-center states of Eq. (6) is truncated[16] to those N strongly coupled by the off-Γ perturbation ($\propto k$) in Eq. (7). Equation (7) becomes an $N\times N$ matrix, the elements of which include terms through second order in Cartesian components of k. For a III-V zinc-blende semiconductor, the three p-derived valence states degenerate at Γ are usually augmented by the first conduction state at Γ. Including spin-orbit effects doubles the number of states retained to 8; this we shall term the "eight-band bulk $\mathbf{k}\cdot\mathbf{p}$ model," used below. Conventional Luttinger parameters $\{\gamma_j\}$ (Appendix) are linear combinations of the $\{\mathbf{p}_{n,n'}\}$ renormalized by Löwdin perturbation theory and simplified using symmetry.[17]

(2) *Fitting.* Had one calculated the $\{\mathbf{p}_{n,n'}\}$ of Eq. (8), or with Luttinger parameters, the band structure could have been predicted for specified $\mathbf{k}$ by diagonalizing Eq. (7). Analytic second k derivatives of the resulting band eigenvalues $\varepsilon_n(\mathbf{k})$, evaluated at Γ, would yield band effective masses in terms of the these parameters. Unless N of Eq. (6) is large enough,[17] however, band properties can be very poor;[18] such effects have been partially examined[19–21] within the $\mathbf{k}\cdot\mathbf{p}$ approach. The severity of the N truncation[20] in (i) is mitigated by the central feature of conventional $\mathbf{k}\cdot\mathbf{p}$ approaches: instead of *computing* the $\{\mathbf{p}_{n,n'}\}$ or $\{\gamma_j\}$—which reflect the atomistic crystal potential $V(\mathbf{r})$—they are *fit* to observed band properties,[22] such as the band gap and [001] and [111] band masses at Γ. The basis truncation above has the following important *physical* consequences: (i) nonparabolicity is difficult to treat systematically, so that bands of pure bulk materials will be valid, in principle, only "near" the Γ point; (ii) bands generally cease to obey Bloch symmetries, such as $\varepsilon_n(\mathbf{k}+\mathbf{G})=\varepsilon_n(\mathbf{k})$ for band n and reciprocal lattice vector $\mathbf{G}$. This often introduces unphysical "out of zone" solutions, which must be detected and eliminated;[23] (iii) bands which do not derive from the zinc-blende Γ point are poorly described. The inadequacy of an $N=8$ basis means that a conventional $\mathbf{k}\cdot\mathbf{p}$ prediction for, e.g., the lowest GaAs conduction band at X would be so high in energy as to be physically meaningless (see Fig. 2 below). An additional set of restrictions on the standard model follow from the conventional description of *heterostructures*, described next.

B. Describing heterostructures

The parametrization of Sec. II A may be applied to each of the materials A and B making up an A/B heterostructure. For a spatially inhomogeneous system, most $\mathbf{k}\cdot\mathbf{p}$+EFA approaches are based on the formalism of Luttinger and Kohn,[15] which treated the response of a homogeneous crystal to a weak, slowly varying external perturbing potential. Un-

der flat band conditions, the A and B regions are assumed bulklike, and the wave function, e.g., in material A, takes the form

$$\psi(\mathbf{r})=\sum_{n=1}^{N} F_n^A(\mathbf{r})u_{n\Gamma}^A(\mathbf{r}), \tag{9}$$

where the $F_n^A(\mathbf{r})$ are envelope functions and the zone-center states $\{u_{n\Gamma}(\mathbf{r})\}$ are formally different in materials A and B. The sum runs over the N states retained in the $\mathbf{k}\cdot\mathbf{p}$ description, defining a multiband EFA. By construction,[15,24] the F_n have Fourier components restricted to the first Brillouin zone of the A or B constituents and are thus fairly *slowly varying*. The derivation of the partial differential equations and boundary conditions obeyed by the envelope functions are thoroughly reviewed by Burt.[24] Virtually all $\mathbf{k}\cdot\mathbf{p}$+EFA calculations have of necessity assumed the *same* set $\{u_{n\Gamma}(\mathbf{r})\}$ of zone-center states in both materials.[24] In the flat band approximation, one recovers a Schrödinger-like equation of the form[25]

$$\sum_{n=1}^{N} H(\mathbf{r},\mathbf{k})_{nm}F_m(\mathbf{r})=\varepsilon F_n(\mathbf{r}). \tag{10}$$

Here the argument $\mathbf{r}$ indicates simply that material parameters depend on the chemical identity of the heterostructure region. A piecewise constant functional form is usually assumed for lamellar systems. In a *bulk* material, k_j is identified as a component of the specified Bloch wave vector; in a *heterostructure*, the replacement[15] $k_j\rightarrow -i\nabla_j$ converts Eq. (10) into a system of N coupled partial differential equations. The prescription for guaranteeing a Hermitian matrix when materials parameters depend on position, and the appropriate boundary conditions to be imposed at interfaces, are reviewed in Ref. 25.

The conventional EFA thus introduces additional restrictions on the physical description: (i) The envelope functions should be slowly varying. This assumption may be violated for sufficiently thin heterostructures, raising questions about accuracy. (ii) The assumption of a weak, slowly varying perturbation would appear dubious in abrupt A/B semiconductor heterostructures and short-period superlattices. (iii) Neglect of *differences* in the zone-center states $\{u_{n\Gamma}(\mathbf{r})\}$ in A and B appears to limit[26] the EFA to heterostructures of electronically similar materials.

III. CALCULATIONAL APPROACH

A. Strategy

The procedure we use to compare, on an entirely equivalent footing, results of the "direct" approach [Eqs. (1)–(4)] with those of the $\mathbf{k}\cdot\mathbf{p}$+EFA "standard model" [Eqs. (7)–(9)] is as follows. *First*, we use the direct approach, implemented within the empirical pseudopotential method, to compute band structures, including band gaps, effective masses, and spin-orbit splittings, for *bulk* GaAs and AlAs. The choice of modern empirical pseudopotentials to describe the atoms in the primitive cell is an issue of implementation, not of principle. The small lattice mismatch between these materials was neglected in all calculations, eliminating the need to specify deformation potentials and elastic properties. *Second*, we equate pseudopotential *calculated* effective masses with their formal expressions in the 8×8 Kane model and extract Luttinger parameters (see the Appendix). These suffice to specify all matrix elements used for $\mathbf{k}\cdot\mathbf{p}$ calculations within the standard 8×8 model. *Finally*, we use these pseudopotential-derived Luttinger parameters and gaps as input to $\mathbf{k}\cdot\mathbf{p}$+EFA calculations of band structures and envelope functions for $(\mathrm{AlAs})_n(\mathrm{GaAs})_n$ superlattices and $(\mathrm{GaAs})_n$/AlAs quantum wells. The results are compared with direct pseudopotential calculations [Eqs. (1)–(4)] for the same structures. Computational details are given below.

B. Direct method: Computational details

Pseudopotentials. For the screened atomic pseudopotentials $v_i(\mathbf{r})$ in Eq. (2), we use the recently developed empirical pseudopotentials of Mäder and Zunger[2] for Ga, Al, and As. These properly include the spin-orbit interaction and have the following properties:[2] (i) they adequately reproduce measured electronic properties of bulk GaAs and AlAs and the scattering properties of Ga and Al in a variety of environments; (ii) wave functions are close to self-consistent local density approximation computed wave functions; (iii) they permit an absolute energy scale, so we may refer heterostructure eigenvalues to those in GaAs by simple subtraction. $\mathbf{k}\cdot\mathbf{p}$+EFA calculations naturally refer heterostructure energy levels to the band edges of the pure constituents; (iv) the As potential depends on the number of Ga and Al nearest neighbors, thereby including most charge transfer and interface effects; and (v) they are algebraically simple even when including the spin-orbit interaction.

Geometries. In the calculations reported below, we consider $(\mathrm{AlAs})_n(\mathrm{GaAs})_n$ superlattices (with $1\leqslant n\leqslant 20$) and $(\mathrm{GaAs})_n$/AlAs quantum wells (with $1\leqslant n\leqslant 10$) based on [001]-orientation tetragonal unit cells. To represent GaAs quantum wells in an AlAs barrier, we use periodic $(\mathrm{GaAs})_n(\mathrm{AlAs})_m$ superlattices with m large enough to effectively isolate GaAs wells. Note that $n+m$ must be *even* for a perfect [001] superlattice described via a *tetragonal* cell: assume that we occupy primitive cell p of an [001] $(AC)_m(BC)_n$ superlattice of cations A and B and anions C in accordance with tetrahedral coordination. This works for $n+m=$even, but for $n+m$ odd, the last anion layer in cell p will be directly below the first anion layer in cell $p+1$, inconsistent with tetrahedral coordination for the first cation layer in cell $p+1$. This defect would introduce spurious impurity levels in the gap; thus, m must be odd (even) if n is odd (even). We use $m=20$ for even n and $m=19$ for odd n. To verify convergence with m for, e.g., $(\mathrm{GaAs})_5(\mathrm{AlAs})_{19}$, we examined the spurious bandwidths of the lowest conduction and highest valence bands along the line between the zone center and zone edge along the [001] direction (Fig. 1). These are <0.2 meV and <0.02 meV, respectively, and this choice for m is thus large enough to remove numerical artifacts of the supercell geometry for near-edge bands.

Method of direct solution. A conjugate gradient program, using a plane wave basis and the pseudopotentials described above, was used to solve Eqs. (1)–(3). The only convergence parameter is the number of plane waves used to describe the Bloch wave function [Eq. (4)]; a kinetic energy cutoff $G_{\max}^2=5$ Ry was used. This direct approach suffers from none of the restrictions to which the standard model is sub-

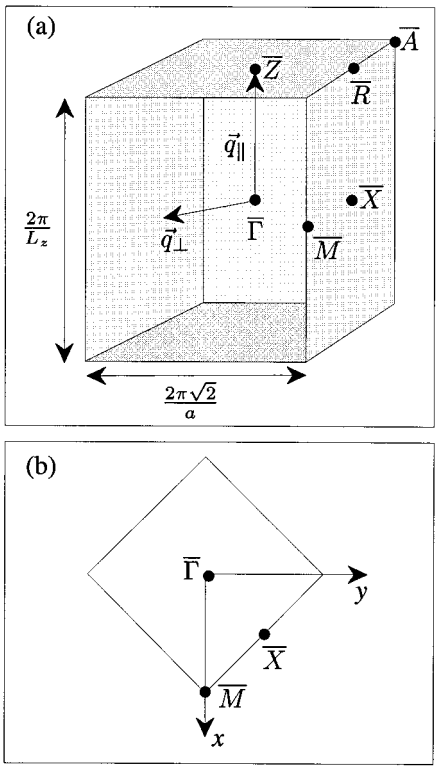

FIG. 1. Brillouin zone for tetragonal description of GaAs-AlAs [001] superlattices and quantum wells. Panel (a) shows high-symmetry points and panel (b) the orientation of x and y axes with respect to the prism cross section. The crystal primitive cell along the z axis is of length L_z, and a is the zinc-blende lattice constant.

ject. In particular, (a) since zinc-blende GaAs and AlAs are correctly described throughout the zinc-blende Brillouin zone, heterostructure X-derived bands will also be correctly described; (b) band dispersion throughout the heterostructure Brillouin zone may be computed with the same accuracy as for a zinc-blende material, since we use a fixed plane wave cutoff; (c) all features of wave functions, with oscillations of all wavelengths permitted by Bloch's theorem, are included; (d) for a specified wave vector **q**, all bands—not simply those which are derived directly from the three valence band and one conduction-band state retained in the 8×8 $\mathbf{k}\cdot\mathbf{p}$ description—may be examined. For these reasons, we refer to the direct calculations below as an ''all band pseudopotential'' or ABP approach.

C. The standard model: Computational details

We use an 8×8 $\mathbf{k}\cdot\mathbf{p}$+EFA method described in detail by Baraff and Gershoni[25] and reviewed by Gershoni *et al.*,[22] but use Luttinger parameters fit to our *calculated* pseudopotential bulk bands for GaAs and AlAs; see the Appendix. Pseudopotential-derived Luttinger parameters and effective masses differ somewhat from accepted values,[22,27,28] although the range of the latter may be large.[28] Our purpose is to compare in detail predictions of two *theoretical* approaches, using precisely equivalent inputs, not to exactly reproduce experimental data.

In the formalism of Baraff and Gershoni,[25] the wave function of the heterostructure is of the form in Eq. (9), where the eight zone-center states $\{u_{n\Gamma}(\mathbf{r})\}$, in principle, differ in GaAs and AlAs. These differences are retained insofar as they enter matrix elements and affect, via material parameters, boundary conditions at interfaces between the two materials,[25] but are not included otherwise. The Kane parameter[8] B', identically zero for systems with inversion symmetry, is assumed zero. The envelope function for band n is expanded for *both* A and B regions in supercell reciprocal lattice vectors appropriate to rectangular geometry:

$$F_n(\mathbf{r})=\sum_{jlm}^{N_xN_yN_z} F_{jlm}^{(n)}\frac{1}{\sqrt{L_xL_yL_z}} \times\exp[2\pi i(jx/L_x+ly/L_y+mz/L_z)], \quad (11)$$

relying on Fourier representability to include the jump discontinuities in material properties at A/B interfaces. The boundary conditions applied to Eqs. (9) and (10) are discussed in detail in Refs. 22 and 25. Since the F_n are in general complex, both oscillatory and decaying contributions to each envelope function are naturally included, circumventing the need to explicitly include both.[29] For all of the geometries we consider, the system is uniform transverse to the superlattice or quantum well stacking direction, so the dimensions L_x and L_y are irrelevant and convergence is determined only by the number of Fourier components N_z retained. For specified **k**, superlattice band energies and envelope functions are found from eigenvalues and eigenvectors of an $8N_z$ square matrix. We have used $N_z=75$; even for the extreme short-period $(\mathrm{AlAs})_1(\mathrm{GaAs})_1$ superlattice, eigenvalues change by less than 0.2 meV on reducing N_z to 25.

IV. COMPARISONS OF "STANDARD MODEL" AND DIRECT CALCULATIONS

[001] $(\mathrm{AlAs})_n(\mathrm{GaAs})_n$ superlattices and $(\mathrm{GaAs})_n$/AlAs quantum wells are conveniently described as tetragonal primitive cells. The Brillouin zone is shown in Fig. 1, where we use an overbar to indicate heterostructure states. We specify band energies for *bulk* zinc-blende AlAs and GaAs using conventional double group, i.e., relativistic, notation, but label heterostructure states via the zinc-blende Brillouin zone point from which they derive. The state $\overline{\Gamma}(X_z)$, for instance, is an [001] heterostructure state at the tetragonal zone center $\overline{\Gamma}$ derived from a zinc-blende X point state, which folds to $\overline{\Gamma}$ due to the longer [001] repeat distance. An arbitrary wave vector **q** in the tetragonal zone can be resolved into components $\mathbf{q}_{\|}$ *along* the stacking direction and an (''in-plane'') component $\mathbf{q}_{\perp}$ *perpendicular* to it. The zinc-blende L point folds[30] to the tetragonal $\overline{X}$ point for even n and to $\overline{R}$ for odd n, while the tetragonal $\overline{M}$ points are derived from the zinc-blende X points in the x-y plane. We use below the notation SM to indicate standard model eight-band $\mathbf{k}\cdot\mathbf{p}$+EFA results and ABP to indicate those of our direct, all band pseudopotential calculations.

A. Bands of bulk GaAs and AlAs

Since we consider [001]-based heterostructures, we examine first the bands of *bulk* GaAs and AlAs along the zinc-blende Γ-X[001] direction. Figure 2 shows the bands of AlAs and GaAs obtained from direct pseudopotential calcu-

lations (solid lines) and within the eight-band $\mathbf{k}\cdot\mathbf{p}$ approach (dashes), using pseudopotential-determined Luttinger parameters. On this scale, $\mathbf{k}\cdot\mathbf{p}$ results appear parabolic; for GaAs, they agree with the correct dispersion of ABP bands to within 50 meV only up to 12%, 18%, 14%, and 14% of the distance toward X for the electron, heavy-hole, light-hole, and split-off bands, respectively; yet larger discrepancies occur farther from Γ. In particular, the GaAs $\mathbf{k}\cdot\mathbf{p}$ X_{6c} state is 26 eV higher than the correct ABP value, so that any $\Gamma_{6c}-X_{6c}$ coupling is unphysically negligible in $\mathbf{k}\cdot\mathbf{p}$.

B. ABP electronic structure of $(AlAs)_n(GaAs)_n$[001] superlattices

We begin by establishing overall trends with n for [001] $(AlAs)_n(GaAs)_n$ conduction-band states, using pseudopotential results (Fig. 3). We note the following.

(i) At the $(AlAs)_n(GaAs)_n$ superlattice zone center, $\overline{\Gamma}(\Gamma_{6c})$ states derive mostly from the zinc-blende GaAs conduction-band minimum Γ_{6c} state, while $\overline{\Gamma}(X_z)$ states derive mostly[30] from the zinc-blende first $X_{6c,z}$ and second $X_{7c,z}$ conduction states at X. For even (odd) n $\overline{\Gamma}(X_{6c,z})$ $[\overline{\Gamma}(X_{7c,z})]$ states have the same symmetry as the $\overline{\Gamma}(\Gamma_{6c})$ state, so they couple and repel one another.[30] Since zinc-blende X_{7c} states lie >0.5 eV higher in energy, symmetry effects are most pronounced for even n. Because zinc-blende X states are all higher in energy than the GaAs Γ_{6c} state, this coupling pushes *down* the $\overline{\Gamma}(\Gamma_{6c})$ state. This opposes the *upward* shift due to confinement (approximately $\propto 1/n^2$). This competition between potential (symmetry) and kinetic effects results in a bending over of the $\overline{\Gamma}(\Gamma_{6c})$ state and a nonmonotonic $\overline{\Gamma}(X_z)/\overline{\Gamma}(\Gamma_{6c})$ splitting for small n. Repulsion with the higher energy $\overline{\Gamma}(X_{7c,z})$ state (not shown) strongly depresses the energy of the $\overline{\Gamma}(\Gamma_{6c})$ state for $n=1$. Symmetry-induced repulsions rapidly attenuate as n increases and confinement effects dominate.

(ii) A transition from $\overline{\Gamma}(X_z)$ to $\overline{\Gamma}(\Gamma_{6c})$ as the lowest conduction band occurs near the critical period[31,32] $n_c=7$, as indicated by the gray circle (experimentally this cross over is found[33] near $n=11$, but the degree of interfacial abruptness is unclear). Figure 4 shows the square moduli of wave functions for the valence-band maximum (VBM) and conduction-band minimum (CBM) at $\overline{\Gamma}$ on either side of this transition. We display such results averaged over the transverse dimensions of the primitive cell, to facilitate later com-

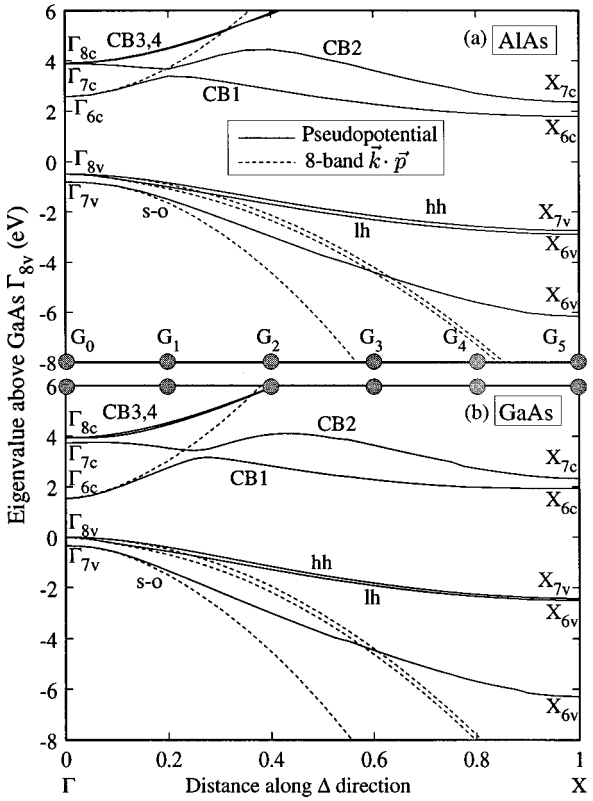

FIG. 2. Dispersion of bulk AlAs and GaAs bands between the zinc-blende Γ and X points (Δ direction): ABP calculations (full lines) and eight-band $\mathbf{k}\cdot\mathbf{p}$ (dashes). Relativistic labels at Γ and X and conventional names for valence bands are used. Note quasiparabolic behavior of $\mathbf{k}\cdot\mathbf{p}$ bands. Gray filled circles show reciprocal lattice vectors, which for the $(AlAs)_5(GaAs)_5$ superlattice fold to the superlattice zone center $\overline{\Gamma}$.

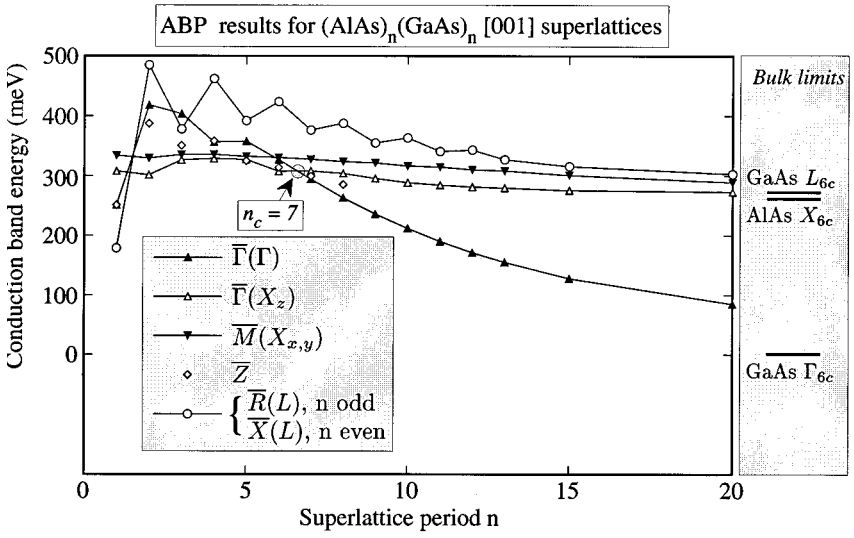

FIG. 3. All band pseudopotential (ABP) conduction-band energies for [001] $(AlAs)_n(GaAs)_n$ superlattices at high-symmetry points (see Fig. 1) as a function of period n. Overbars indicate superlattice states, which derive from the zinc-blende state given in parentheses. Band energies for *bulk* AlAs and GaAs (Fig. 2) appropriate to the limit $n\to\infty$ are given at right. The energy zero is taken at the bulk GaAs conduction-band minimum Γ_{6c} state. A transition from $\overline{\Gamma}(X_z)$ to $\overline{\Gamma}(\Gamma_{6c})$ as the lowest conduction band occurs near the critical period $n_c=7$ (gray circle).

parisons with envelope functions. We note that (a) for $n=7$ both electrons and holes are localized primarily within the GaAs region, while for $n=6$ electrons are found with comparable probabilities in both regions. For $n<6$ (not shown) the CBM is more strongly localized in the AlAs region, while the VBM remains GaAs-like, confirming that this band crossing marks a transition for the GaAs/AlAs system from a type II (electrons and holes localized in different spatial regions) to a type I superlattice (electrons and holes localized in the same spatial region). Also, (b) the CBM shows prominent peaks[34] (indicated by asterisks) near GaAs/AlAs interfaces.

(iii) The nonfolding $\bar{M}(X_{x,y})$ states shown in Fig. 3 are relatively insensitive to n and slowly approach the bulk AlAs X_{6c} state for very large n.

(iv) The zinc-blende L-derived points $\bar{R}(L)$ (for odd n) and $\bar{X}(L)$ (for even n) oscillate[30] strongly for small n and asymptotically approach the GaAs L_{6c} conduction-band minimum for large n.

(v) The $n=1$ superlattice is indirect via the $\bar{R}$ point, while the $n=2$, 3, 4, and 6 superlattices are pseudodirect via the $\bar{\Gamma}(X_z)$ point, coupled to the VBM by weak dipole matrix elements typical of folded-in states. Curiously, for $n=5$, the $\bar{Z}$ point, 2.3 meV below $\bar{\Gamma}(X_z)$, is the conduction-band minimum.

Effects (i)–(v) are *all absent from the "standard model."* In particular, the nonmonotonic dependence of band energies on n [(i) and (iv) above] is mandated in the pseudopotential approach by changes in point group symmetries[11] with n. Input parameters to the two classes of calculations emphasize profound physical differences in the symmetries retained: The ABP approach requires specification of microscopic atomistic quantities, i.e., primitive translation vectors for the structure, the identity and coordinates of all atoms within the primitive cell, and pseudopotentials for all distinct atom types. Standard model calculations require only the heterostructure orientation and *continuum* properties: the length of each region, and material parameters for pure GaAs and AlAs. The standard model is thus entirely oblivious to even/odd symmetries and their effects on energetics. It would, moreover, accept without protest geometries which in an atomistic description would yield defect levels in the gap [e.g., [001] $(AlAs)_m(GaAs)_n$ superlattices with tetragonal unit cells for $m+n$ odd, discussed in Sec. III B].

We emphasize that the standard model describes adequately only the $\bar{\Gamma}(\Gamma_{6c})$ conduction states; X- and L-derived states ($\bar{M}$, $\bar{R}$, and $\bar{X}$ in Fig. 3) are so high in energy as to be absent. Since $\bar{\Gamma}(\Gamma_{6c})$ is the conduction-band minimum only for $n\geq 7$, only for such n can SM predictions be *qualitatively* correct. The extent to which there is *quantitative* agreement for this range is established in the next section.

C. ABP and standard model predictions for [001] superlattices

1. Band energies at $\bar{\Gamma}$

Figure 5 compares ABP and SM near-edge band energies at $\bar{\Gamma}$ for $(AlAs)_n(GaAs)_n$ superlattices as a function of n.

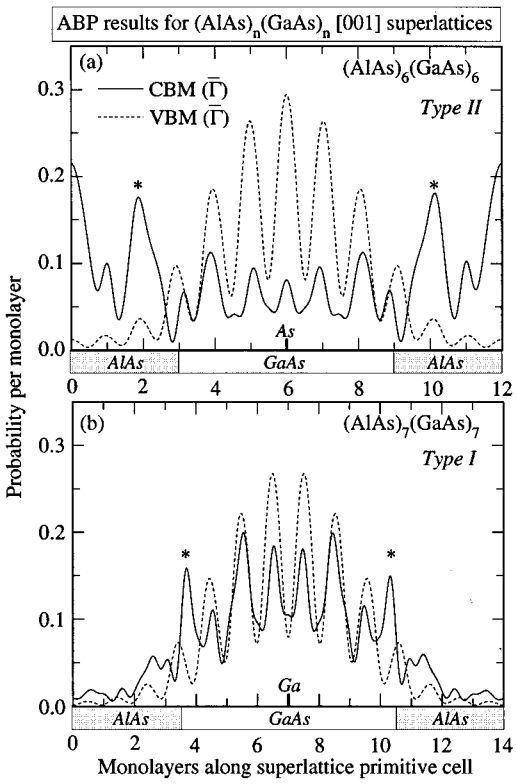

FIG. 4. Zone-center ABP wave functions on either side of the $\bar{\Gamma}(X_z)$ to $\bar{\Gamma}(\Gamma_{6c})$ crossing for [001] $(AlAs)_n(GaAs)_n$ superlattices. Solid lines depict planar-averaged square moduli of the conduction-band minimum (CBM) Bloch state, while dashed lines show corresponding quantity for the valence-band maximum (VBM) hh1 state; normalization is chosen to give probability per monolayer. For $n=7$ [panel (b)] electrons and holes are both localized primarily within the GaAs region, while for $n=6$ [panel (a)], electrons are found with a greater probability in the AlAs regions. Integer monolayer labels correspond to As (Ga/Al) layers for $n=6$ ($n=7$). For electron states, note prominent peaks near interfaces (asterisks).

Relevant band energies of the bulk constituents are shown at right. For conduction bands only the lowest $\bar{\Gamma}(\Gamma_{6c})$ and $\bar{\Gamma}(X_z)$ states are shown.

We find that (i) the standard model *misses* several additional, folded-in electron states (discussed below)in the energy window; (ii) the symmetry-induced nonmonotonicity (Sec. IV B) in the ABP $\bar{\Gamma}(\Gamma_{6c})$ curve for small n is beyond the reach of the SM; and (iii) the SM overestimates the energy of the $\bar{\Gamma}(\Gamma_{6c})$ state by an amount shown by the shaded region in panel (a).

For *valence bands* with a binding energy $\lesssim 200$ meV agreement between SM and ABP calculations is very good: (i) the ABP hh1/lh1 splitting, including a maximum at $n\simeq 9$, is very closely tracked, although (ii) the first SM split-off s-o state lies 6–8 meV below the corresponding ABP curve for all n, except near band crossings, and crosses the hh2 state between $n=5$ and $n=6$ in the ABP calculations, but shifts up by 1 ML in SM calculations; (iii) for $n\gtrsim 10$, agreement for the hh2 state is also very good, though by $n=5$, it is ~ 80 meV too low in the SM; (iv) deeper into the valence-band SM energies are *too deep*.

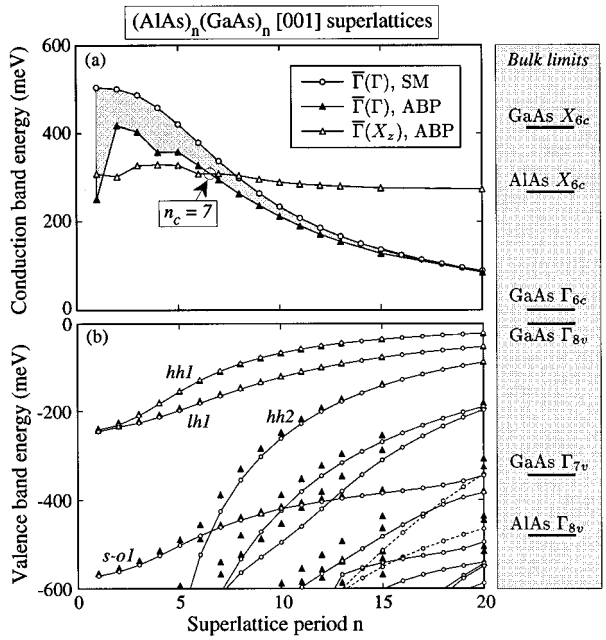

FIG. 5. Comparison of ABP and SM band energies for $(AlAs)_n(GaAs)_n$ superlattices. Only the lowest $\overline{\Gamma}(\Gamma_{6c})$ and $\overline{\Gamma}(X_z)$ conduction and near-edge valence bands are shown as a function of n. Shading in (a) indicates SM error for $\overline{\Gamma}(\Gamma_{6c})$ state. Dashed lines [panel (b), lower right] show band connectivity near crossings.

2. Near-edge wave functions at $\overline{\Gamma}$

Is the good agreement between the pseudopotential and the standard model approaches for near-edge hole states, but poor agreement for the $\overline{\Gamma}(\Gamma_{6c})$ state, reflected in the quality of the corresponding wave functions? Figure 6 shows the square moduli of wave functions for the $\overline{\Gamma}(\Gamma_{6c})$ electron state and near-edge hole states at $\overline{\Gamma}$ for $n=5$ (left column) and $n=10$ (right column); ABP planar-averaged wave functions are shown as solid lines. For states whose *energy* (Fig. 5) is well described by the standard model envelope functions closely average the upper and lower envelopes of Bloch states. The obvious exception is the $n=5$ $\overline{\Gamma}(\Gamma_{6c})$ electron state, for which the ABP wave function shows prominent interfacial peaks (indicated by asterisks in Figs. 4 and 6) absent from the SM.

3. In-plane and out of plane band dispersion

Since finite-temperature measurements and optical spectroscopy probe a finite region about the zone center, we next consider band dispersion away from $\overline{\Gamma}$. Using the notation of Fig. 1, we examine dispersion for wave vectors $\mathbf{q}_\parallel$ along the superlattice repeat (z) axis and in-plane wave vectors $\mathbf{q}_\perp$ perpendicular to it.

Figure 7 compares, for $\mathbf{q}_\perp \equiv 0$, dispersion of near-edge bands between the $\overline{\Gamma}$ and Z points of the tetragonal Brillouin zone for the $(AlAs)_5(GaAs)_5$ superlattice, below the type II to type I transition described above. In this direction, the spin degeneracy is preserved, i.e., each band displayed is twofold degenerate. In the energy window shown, (i) there are three additional conduction bands missing from the SM, because of its gross overestimate of folded-in $\overline{\Gamma}(\Delta)$ state energies.

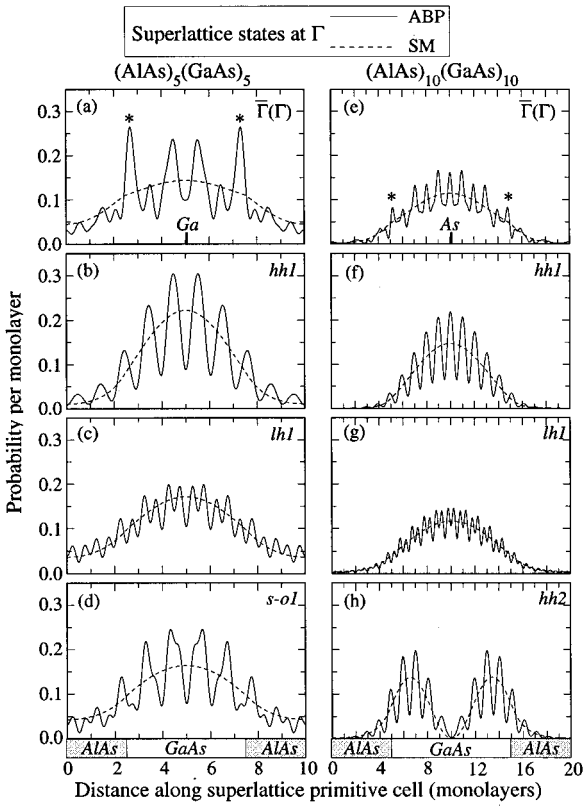

FIG. 6. Square moduli of Bloch states and envelope functions for near-edge states at $\overline{\Gamma}$ for $(AlAs)_5(GaAs)_5$ (left column) and $(AlAs)_{10}(GaAs)_{10}$ (right column) superlattices predicted from ABP (solid lines) or standard model (SM, dashed lines) calculations. Panels in each column are in order of decreasing band energy; note correspondence with sequence in Fig. 5. A spatial overtone structure characteristic of the zinc-blende state from which superlattice states derive is evident in heavy-hole, light-hole, and split-off ABP wave functions. Odd (even) n superlattices have inversion symmetry about planes containing Ga (As) atoms. Note peaks on GaAs side of interfaces for electron states (asterisks).

The qualitative nature of each band at $\overline{\Gamma}$ is labeled G (primarily GaAs-like), A (primarily AlAs-like), or M (mixed over both regions); (ii) there is a $\sim$65 meV upward shift (see Fig. 5) of the $\overline{\Gamma}(\Gamma_{6c})$ state, although its dispersion is well described by the SM for $q_\parallel a/2\pi \lesssim 0.05$; (iii) while the dispersion of the lh1 and hh1 valence bands [panel (b)] is well described up to the zone boundary, the ABP split-off (s-$o1$) and hh2 bands show an avoided crossing at $q_\parallel a/2\pi \simeq 0.04$ which occurs in the SM as a simple crossing at $q_\parallel a/2\pi \simeq 0.055$; (iv) the hh2 band, $\sim$80 meV too deep at $\overline{\Gamma}$ in the SM (Fig. 5), is $\sim$40 meV too deep at $\overline{Z}$.

Band dispersion as $\mathbf{q}_\perp$ moves toward the M point (for $q_\parallel \equiv 0$) is shown in Fig. 8. In this direction symmetry permits the lifting of the spin-up vs spin-down degeneracy, resulting in a doubling of the number of ABP bands seen in Fig. 7. With our Kane parameter choice[35] $B' \equiv 0$, however, this degeneracy is *not* lifted in the standard model. Unlike along the $\overline{\Gamma} \rightarrow \overline{Z}$ line (Fig. 7), conduction bands all disperse quadratically, despite a band crossing at $q_\perp a/2\pi \simeq 0.05$. The hh1 bandwidth [panel (b)] is much greater than toward $\overline{Z}$, and, as for the s-$o1$ band, is strongly split by the spin-orbit interac-

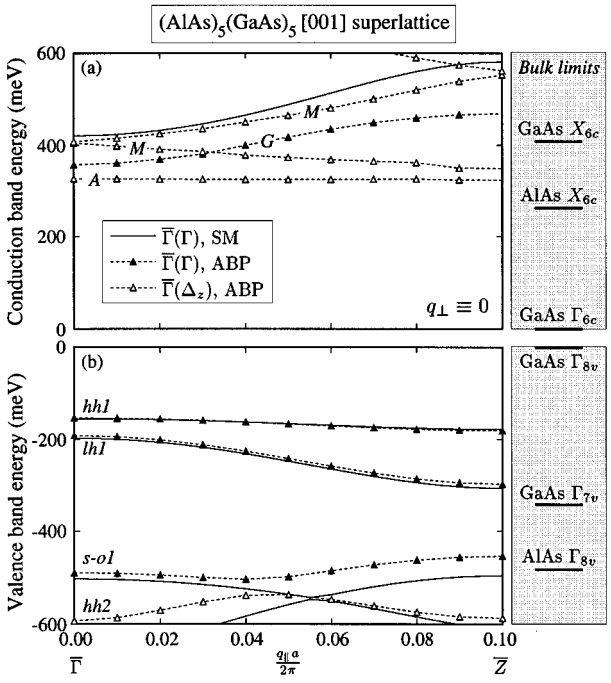

FIG. 7. For $(AlAs)_5(GaAs)_5$ superlattice, comparison of ABP and SM dispersion of near-edge conduction and valence bands between $\bar{\Gamma}$ and $\bar{Z}$ points of tetragonal Brillouin zone (see Fig. 1). In this direction, the spin degeneracy is preserved, i.e., each band displayed is twofold degenerate. Open triangles indicate states which are derived from zinc-blende states folded in from the Δ direction. For electron states, *G* and *A* indicate localization primarily in GaAs or AlAs, while *M* indicates substantial mixing over both regions.

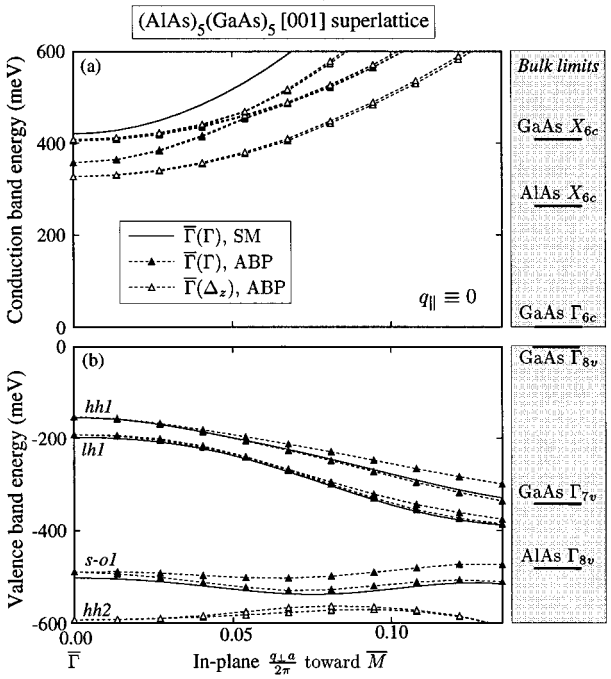

FIG. 8. In-plane dispersion of near-edge conduction and valence bands toward $\bar{M}$ from the $\bar{\Gamma}$ point of the tetragonal Brillouin zone for $(AlAs)_5(GaAs)_5$ superlattice. The spin degeneracy is broken in this direction in ABP (but not SM) calculations; symbols are as in Fig. 7.

tion. In contrasting ABP and the SM, we note that (i) the spin splitting is nonzero and significant in the ABP results for valence bands;[35] (ii) apart from the shift discussed earlier, once again, dispersion of the $\bar{\Gamma}(\Gamma_{6c})$ electron band is well described for $q_\perp a/2\pi \lesssim 0.05$; (iii) despite an underestimate of the band energy which increases with $q_\perp$, the SM reproduces a shallow minimum of the *s-o*1 band at $q_\perp a/2\pi \simeq 0.08$; (iv) even for $n=5$, band dispersion is quite anisotropic. The ABP values for $m_\parallel/m_\perp$ at $\bar{\Gamma}$ are, for example, $\simeq 3.4$ for the hh1 state and $\simeq 0.95$ for the $\bar{\Gamma}(\Gamma_{6c})$ electron state. The corresponding SM values are 4.4 and 1.3, respectively; the anisotropy of effective masses is thus exaggerated within the SM.

Bands for the $(AlAs)_{10}(GaAs)_{10}$ superlattice naturally show much less dispersion with $q_\parallel$ (not shown) than for the $(AlAs)_5(GaAs)_5$ case. Figure 9 shows better agreement between SM and ABP results for $q_\perp$ (in-plane) dispersion of valence bands, primarily because ABP spin-orbit splittings are smaller for the $(AlAs)_{10}(GaAs)_{10}$ case, similar to the large-*n* damping of odd-even *n* oscillations for conduction-band states seen in Fig. 3.

Based on the calculations for $(AlAs)_n(GaAs)_n$ superlattices presented above, we may conclude that (i) for hh1 and lh1 bands, except for complete omission of spin splittings with in-plane dispersion, the standard model closely reproduces ABP results. Substantial ABP-predicted spin splittings of the *s-o*1 band for $q_\perp \neq 0$ may be experimentally detectable and represent a significant error in the standard model even for *hole* bands; (ii) for electron bands, agreement is generally restricted to a region about the $\bar{\Gamma}$ point, with a systematic overestimate of the $\bar{\Gamma}(\Gamma_{6c})$ state exceeding 20 meV for $n=10$, but falling to less than 4 meV for $n=20$. All *X*-derived states are missed for all *n*.

D. ABP and standard model predictions for quantum wells

We have also carried out detailed ABP and eight-band $\mathbf{k}\cdot\mathbf{p}$+EFA standard model calculations for $(GaAs)_n$/AlAs quantum wells; for small *n*, these model the properties of *isovalent* "δ-layer" systems. These represent a more stringent test of the standard model because the AlAs X_{6c} state, which now dominates confinement in the system, will be poorly described by $\mathbf{k}\cdot\mathbf{p}$.

1. Band energies at $\bar{\Gamma}$

Figure 10 shows energies at $\bar{\Gamma}$ for $(GaAs)_n$/AlAs quantum wells as a function of the GaAs well thickness *n*, analogous to those for superlattices in Fig. 5. Only the lowest $\bar{\Gamma}(\Gamma_{6c})$ and $\bar{\Gamma}(X_z)$ conduction states are shown. A number of differences with respect to the superlattice case (Fig. 5), are apparent: (i) the lowest $\bar{\Gamma}(X_z)$ conduction band is approximately pinned for all *n* at the energy of the bulk AlAs X_{6c} state, confirming convergence of our description of the quantum well geometry; (ii) this circumstance shifts the crossover of $\bar{\Gamma}(X_z)$ to $\bar{\Gamma}(\Gamma_{6c})$ as the conduction-band minimum from $n_c \simeq 7$ for $(AlAs)_n(GaAs)_n$ superlattices to $n_c \simeq 9$ for $(GaAs)_n$/AlAs quantum wells. Figure 11, analogous to Fig. 4 for superlattices, confirms the corresponding shift to larger *n* of the spatial localization (type II to type I) transition. A

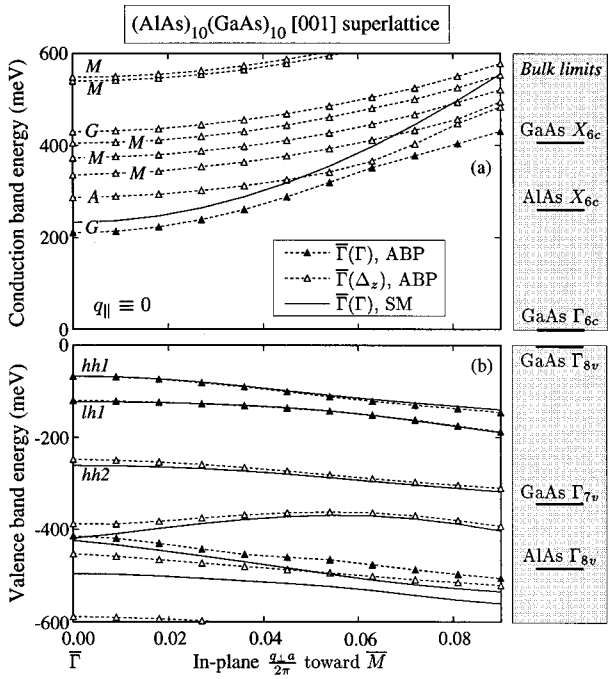

FIG. 9. As in Fig. 8, but for $(AlAs)_{10}(GaAs)_{10}$ superlattice. Note poor SM description of $\overline{\Gamma}(\Gamma_{6c})$ dispersion beyond $q_\perp a/2\pi \simeq 0.05$, but good agreement for near-edge hole states.

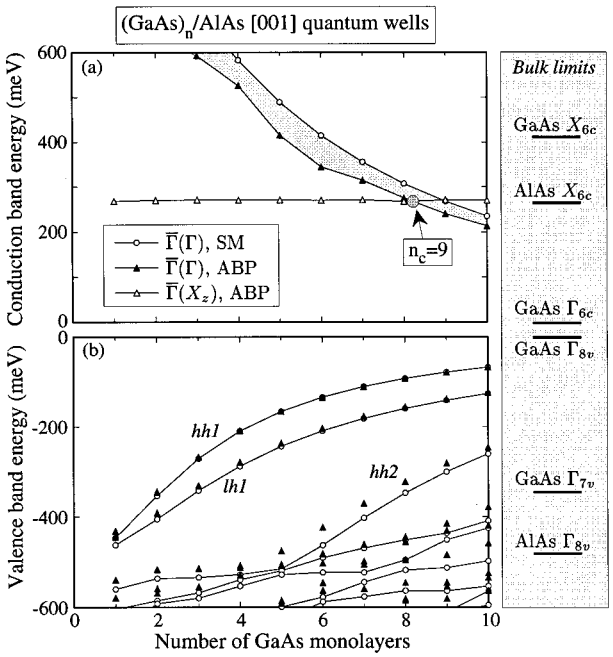

FIG. 10. As in Fig. 5, but for $(GaAs)_n$/AlAs *quantum wells*. Note (i) $\overline{\Gamma}(\Gamma_{6c})$ behavior appreciably different than in Fig. 5; (ii) valence-band behavior generally similar to Fig. 5. The crossing of $\overline{\Gamma}(\Gamma_{6c})$ and $\overline{\Gamma}(X_{6c,z})$ states occurs near $n_c \simeq 9$ (gray circle).

slight increase (with respect to that for the superlattice geometry) in the number of monolayers required for the type II to type I transition for the quantum well geometry has been noted by Mäder, who used an empirical tight-binding Green's function approach;[36] (iii) the energy of the $\overline{\Gamma}(\Gamma_{6c})$ state rises steeply as the quantum well thickness is reduced, while for the superlattice case [Fig. 5(a)] the energy for this state flattens out. This reflects electron confinement in the GaAs well to smaller thicknesses than possible for the superlattice geometry; (iv) valence-band behavior is generally similar to the superlattice case [Fig. 5(b)], except that both hh1 and lh1 states are concave downward functions of n in the quantum well case. Our results are very similar to those of Mäder[36] and of Boring and Gil.[37]

In contrasting ABP and standard model results, it is evident that (i) agreement for valence bands is restricted to the hh1 and lh1 states, except for larger n than shown, and (ii) a systematic overestimate of the $\overline{\Gamma}(\Gamma_{6c})$ state remains.

2. Quantum well band dispersion

As expected when there is very little overlap between GaAs-derived states in adjacent wells, we find virtually no dispersion with $q_\parallel$ for near-edge quantum well bands. Dispersion with the in-plane wave vector component $\mathbf{q}_\perp$, analogous to Fig. 8 for the $(AlAs)_5(GaAs)_5$ superlattice, is shown in Fig. 12. Toward the M point, we find for *conduction* bands that (i) there is a $\sim$75 meV overestimate of the $\overline{\Gamma}(\Gamma_{6c})$ energy; (ii) the SM and ABP give electron effective masses $m^*_{el}/m_0 \simeq 0.14$ and 0.19, respectively, for the $\overline{\Gamma}(\Gamma_{6c})$ state at Γ; (iii) there are several bands folded from the Δ direction completely missing from the SM description.[38] For *valence* bands, we find that (i) close agreement between ABP and SM results for the hh1 and hh2 bands ceases past $q_\perp a/2\pi \simeq 0.05$ or so, due to SM omission of spin-orbit splitting. SM and ABP hh1 effective masses at Γ are 0.32 and 0.38, respectively; (ii) *s-o* and hh2 bands are poorly described by the SM because of strong spin-orbit splitting, although the dispersion of the ABP *s-o* band is tracked.

V. DISCUSSION: ORIGINS OF k·p FAILURES

The specific results for [001] GaAs/AlAs heterostructures above demonstrate the following: For *electron* states, (i) the eight-band **k**·**p**+EFA standard model essentially neglects, because of an inadequate description of dispersion, X- and L-derived states for all superlattice and quantum well thicknesses. This omission makes the SM *qualitatively* wrong for those GaAs/AlAs systems in which X point-derived states constitute the conduction-band minimum; we defer to Sec. VI a more general discussion of its validity. Even if the heterostructure conduction-band minimum derives from zinc-blende Γ points, omission of non-Γ states may be important insofar as they affect interpretation of transport or high pressure properties. Using zinc-blende X- and L-point band energies and masses, one could, in principle, include these states together with Γ states in simple effective mass (one band at a time) calculations. Alternatively, choice of a longer zinc-blende primitive cell (e.g., a doubling along the [001] direction so that the X point would fold to Γ) could be used to append such states to the standard model. However, both approaches do not permit such states to couple to other states. (ii) The SM omits odd-even energy oscillations reflecting discrete crystal symmetries; and (iii) the SM overestimates the energy of the $\overline{\Gamma}(\Gamma_{6c})$ state by an amount which falls with n from hundreds of meV, still exceeding 10 meV

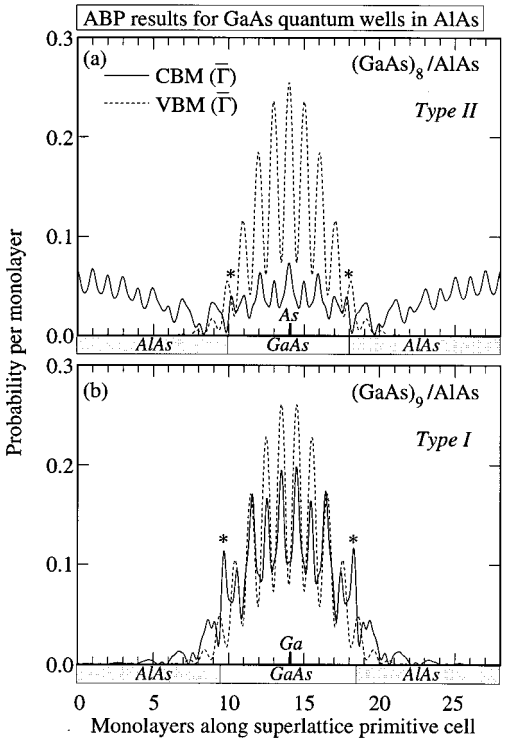

FIG. 11. As in Fig. 4, but for $(GaAs)_n$/AlAs *quantum wells*. Note the shift, with respect to the superlattice case, in the number of GaAs monolayers n required to make the system type I ($n \simeq 9$ vs $n \simeq 7$).

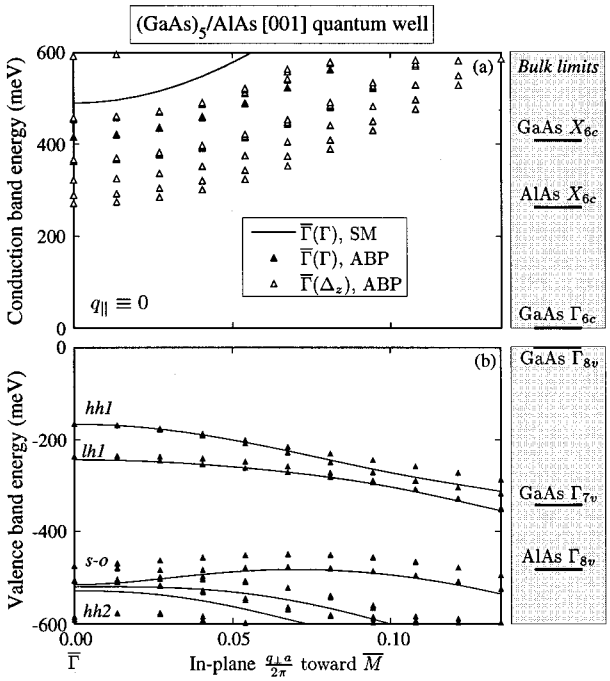

FIG. 12. Dispersion of near-edge conduction and valence bands toward the $\bar{M}$ point from the $\bar{\Gamma}$ point of the tetragonal Brillouin zone for a $(GaAs)_5$/AlAs quantum well. The spin degeneracy is broken in this direction. Note shift in *s-o* SM band, with respect to ABP and poor SM description of hh1 and hh2 dispersion beyond $q_\perp a/2\pi \simeq 0.07$.

until GaAs thicknesses of ~ 40 Å. For *valence* states, (i) the SM is generally good for hh1 and lh1 bands, but deteriorates deeper into the valence band and away from the zone center $\bar{\Gamma}$; (ii) neglects spin splittings when the spin degeneracy is lifted, e.g., for in-plane dispersion. With respect to the ABP, the standard model overestimates electron and hh1 effective masses $m_\parallel$ for dispersion along [001] and underestimates the effective mass $m_\perp$ describing in-plane dispersion.

A. Projections onto zinc-blende states

The standard model attempts to describe A/B heterostructure bands via a small number of bands of the bulk constituents A and B. To analyze the SM failures noted above, we will therefore proceed as follows: *First*, we show how to project superlattice wave functions at $\bar{\Gamma}$ onto a complete set of zinc-blende bands; *second*, we demonstrate this projection technique using computed ABP superlattice wave functions. This establishes the composition of realistic superlattice states using an approach free of the SM errors. *Finally*, we examine the placement of ABP and SM superlattice states in light of this decomposition and the already noted standard model errors for *bulk* GaAs and AlAs.

The decomposition of superlattice wave functions is carried out as follows. $\bar{\Gamma}$ states of an $(AC)_n(BC)_n[001]$ superlattice are derived[39] from zinc-blende states at the *superlattice* reciprocal lattice vectors $G_j = 2\pi j/na$, for $j = 0,1,2,\ldots,n$ along the zinc-blende Γ-X (Δ) line:

$$|\psi_{\bar{\Gamma}}^{\mathrm{SL}}\rangle = \sum_s^{\infty} \sum_{G_j} \alpha_{s,G_j} |\psi_{s,G_j}^{\mathrm{ZB}}\rangle. \tag{12}$$

The $G_{j\neq 0}$ fold to $\bar{\Gamma}$ in the superlattice geometry; these are shown for the $(AlAs)_5(GaAs)_5$ case as gray circles in Fig. 2. The projection on zinc-blende band s at G_j (the state $|\psi_{s,G_j}^{\mathrm{ZB}}\rangle$) is thus

$$P_{sG_j} \equiv |\langle \psi_{\bar{\Gamma}}^{\mathrm{SL}} | \psi_{s,G_j}^{\mathrm{ZB}} \rangle|^2 \equiv |\alpha_{s,G_j}|^2. \tag{13}$$

The net contribution of zinc-blende band s to the projection, is therefore

$$P_s \equiv \sum_{j=0}^{n} P_{sG_j}; \tag{14}$$

P_s thus measures how completely a particular superlattice state derives from zinc-blende band s. If we retain N_b different bands in our description, the quantity

$$P \equiv \sum_{s=1}^{N_b} P_s \tag{15}$$

measures the extent to which the set retained is complete ($P \equiv 1$), i.e., adequately describes the superlattice state. We emphasize the difference between the number of zinc-blende *bands* used in the projections and the number of (Bloch) *states* used. A single zinc-blende *band*, for example, gives rise to $2n$ distinct *states* (or $4n$ including spin splitting) at the superlattice zone center: G_0 and G_n (at the ends of the band in the zinc-blende Δ direction) each occur once, while $G_1 \cdots G_{n-1}$ each occur twice. This "level structure" and the band/state distinction is important to understand errors made by the standard model.

TABLE I. ABP projections P_{sG_j} [Eq. (13)] of superlattice (SL) and quantum well (QW) lowest two conduction states at $\overline{\Gamma}$ (labeled $\overline{\Gamma}^{(1)}$ and $\overline{\Gamma}^{(2)}$) onto zinc-blende GaAs first conduction-band states at Γ and X, labeled "GaAs state projected on." These confirm the crossing of $\overline{\Gamma}(\Gamma_{6c})$ and $\overline{\Gamma}(X_{6c,z})$ states, and an associated type II to type I transition, in each system. GaAs states are labeled as band $s=\mathrm{CB1}(G_j)$ with conventional relativistic labels (Fig. 2) in brackets.

SL state at $\overline{\Gamma}$	GaAs state projected on	n in $(\mathrm{AlAs})_n(\mathrm{GaAs})_n$ SL		n in $(\mathrm{GaAs})_n$/AlAs QW	
		6	7	8	9
$\overline{\Gamma}^{(1)}$	CB1(Γ) [Γ_{6c}]	0.352	0.746	0.148	0.438
$\overline{\Gamma}^{(1)}$	CB1(X) [$X_{6c,z}$]	0.268	<0.001	0.381	<0.002
$\overline{\Gamma}^{(2)}$	CB1(Γ) [Γ_{6c}]	0.290	<0.001	0.263	<0.001
$\overline{\Gamma}^{(2)}$	CB1(X) [$X_{6c,z}$]	0.622	0.699	0.224	0.579

B. Analysis of ABP results via projections

Because near-edge GaAs/AlAs heterostructure states are often derived largely from GaAs bands, for convenience we project on zinc-blende GaAs states. Due to the great similarity of GaAs and AlAs, results would be very similar had AlAs Bloch states been used. We emphasize that a large projection onto GaAs for a superlattice state need *not* imply that the state is necessarily derived from a GaAs state; a comparison of projections onto both GaAs and AlAs states and examination of the wave function would be necessary for this conclusion.

1. Type II to type I transition

The two lowest heterostructure states at $\overline{\Gamma}$ are derived mostly (Fig. 3) from the zinc-blende Γ_{6c} and $\simeq X_{6c,z}$ points. Partial projections onto GaAs Γ and X conduction-band states (i.e., at $G_j=2\pi j/na$ for $j=0$ and $j=n$ only) suffice to confirm the crossing of these two heterostructure states at critical thicknesses shown in Figs. 5 and 10. In Table I, we give such projections for superlattices and quantum wells on either side of the crossing, the signature of which is a sharp increase in the Γ character of the lowest heterostructure conduction band associated with a sharp increase in the X character of the second conduction band. For both superlattices and quantum wells, however, the strongly mixed character of the conduction-band minimum just below the transition, evident in Figs. 4 and 11, is clear from the projections. For smaller n the heterostructures are more clearly type II, with electrons localized in AlAs regions.

2. Character of superlattice states via projections

We use the $(\mathrm{AlAs})_5(\mathrm{GaAs})_5$ superlattice as a detailed example and examine via projections three issues, in order of their quantitative importance: (a) *dispersion* of a projected-on zinc-blende band (see Fig. 2), i.e., P_{sG_j} vs G_j; (b) *mixing* of different zinc-blende bands in the superlattice, measured by $1-P_s$; and (c) *completeness* of the set of zinc-blende bands retained, using the quantity P above. We will project onto $N_b=10$ zinc-blende GaAs bands: the (spin split) first and second conduction bands[40] denoted CB1 and CB2, and the heavy-hole (hh), light-hole (lh), and split-off (s-o) valence bands; these labels are used in Tables II and III. Spin-up and spin-down components of each zinc-blende state both contribute to the projection.[41,42] Table II shows, for the lowest two superlattice conduction states and the highest seven valence states, contributions from the G_j above. The label used for a superlattice state (e.g., hh1) reflects the zinc-blende band (e.g., hh), which dominates its projection: a large value of P_s is *ex post facto* justification for this label.

For superlattice *valence* states at $\overline{\Gamma}$, we find that (i) hh1, lh1, and s-$o1$ states are derived mostly from the zinc-blende Γ point (G_0), while hh2 and lh2 states are derived mostly from G_1, etc., in agreement with the expected level structure discussed above (for hh2 and lh2, we use the labels a and b to distinguish the two superlattice states derived from the G_1 zinc-blende state); (ii) in all cases there are significant contributions from nondominant G_j. hh1, lh1, and s-$o1$ states have monotonically *decreasing* contributions from $G_j\neq 0$, since GaAs valence bands disperse monotonically from Γ [Fig. 2(b)]. (iii) $1-P_s$ exceeds 5% for the s-$o1$ and deeper valence-band states, suggesting that mixing of different zinc-blende bands occurs in these superlattice states.

For superlattice *conduction bands* at $\overline{\Gamma}$, (i) the $\overline{\Gamma}(\Gamma_{6c})$ state has only $a\simeq 80\%$ projection on the GaAs Γ point ($\equiv G_0$), with contributions $\sim 20\%$ as large from other G_j, which depend nonmonotonically on j, reflecting the dispersion of the first ABP conduction band of GaAs; (ii) $1-P_s$ exceeds $\simeq 6\%$ for the $\overline{\Gamma}(\Gamma_{6c})$ state, suggesting higher GaAs conduction-band contributions.

Table III shows, for the same states as in Table II, the quantity P_s [Eq. (14)] describing contributions of *different* zinc-blende bands to a superlattice state, and P [Eq. (15)], measuring basis set completeness. We note that (i) for all nine superlattice states the five GaAs bands included are essentially complete, i.e., P is very near 1; (ii) *mixing* between zinc-blende hh, lh, and s-o states in the superlattice is sufficient to account for virtually all of the $1-P_s$ deficits noted above for deeper superlattice valence states. Thus, heavy-hole, light-hole, and split-off zinc-blende bands suffice to describe superlattice *valence* states very well. (iii) Interestingly, *only* the $\overline{\Gamma}(\Gamma_{6c})$ state—putatively described by $\mathbf{k}\cdot\mathbf{p}$—has an appreciable ($\sim 5\%$) contribution from a state (the GaAs second conduction band) *outside* the set retained in the eight-band $\mathbf{k}\cdot\mathbf{p}$ approach. (iv) Table III also permits partial evaluation of the extent of heavy hole/light hole (interband) mixing in the $(\mathrm{AlAs})_5(\mathrm{GaAs})_5$ superlattice. It is often stated[43] that interfaces in heterostructures cause mixing of bulk valence-band states. Such mixing, however, is *ob-*

TABLE II. ABP projections P_{sG_j} [Eq. (13)] of $(GaAs)_5(AlAs)_5$ superlattice states at $\overline{\Gamma}$ onto zinc-blende GaAs band at $G_j = 2\pi j/5a$ along the Δ (Γ-X) direction. G_0 and G_5 correspond to ZB Γ and X points. The G_j are shown as filled circles in Fig. 2.

GL state	GaAs band	G_0	G_1	G_2	G_3	G_4	G_5	Sum P_s
$\overline{\Gamma}(\Gamma_{6c})$	CB1	0.796	0.083	0	0.047	0.017	0	0.943
$\overline{\Gamma}(X_z)$	CB1	0	0	0.004	0.000	0.032	0.954	0.990
hh1	hh	0.843	0.154	0.001	0.000	0	0	0.998
lh1	lh	0.925	0.057	0	0	0	0	0.982
*s-o*1	*s-o*	0.800	0.008	0	0	0	0	0.808
hh2-*a*	hh	0	0.894	0.039	0	0	0	0.933
hh2-*b*	hh	0.143	0.811	0.016	0.000	0	0	0.970
lh2-*a*	lh	0	0.927	0.020	0	0	0	0.947
lh2-*b*	lh	0.044	0.775	0.010	0	0	0	0.829

served only[44] at finite values of the in-plane wave vector $\mathbf{q}_\perp$, where it is attributed[44] to nonparabolicities of the zinc-blende valence bands. Using an empirical pseudopotential approach, Edwards and Inkson[45] have examined hole states in GaAs/AlAs double barrier and multiple quantum well structures. They find pairs of lh-hh resonances in the transmission coefficient which they trace to the *differences* in the cell-periodic functions $u_{n\Gamma}(\mathbf{r})$ in GaAs and AlAs [see Eq. (9)]. They note that the behavior they find for finite $\mathbf{q}_\perp$ is qualitatively similar to that at $\overline{\Gamma}$, suggesting that mixing is important there. For our calculations at $\overline{\Gamma}$, which fully retain such differences in the GaAs/AlAs $u_{n\Gamma}(\mathbf{r})$, such mixing is extremely small for the hh1 and lh1 states, although the mixed character of deeper valence bands increases.

3. Analysis of standard model errors via projections

The previous section implies that *provided* the dispersion of each bulk band is properly described, as is the case for the pseudopotential GaAs band structure of Fig. 2, a relatively small number of near-edge zinc-blende bands is sufficient to quantitatively describe the heterostructures above in terms of projections. If so, why is the standard model unsatisfactory for superlattice conduction and deep hole bands? Figure 2 and the projections in Table II permit a reassessment of the $\mathbf{k}\cdot\mathbf{p}$+EFA errors noted above. We will show that most errors may be traced simply to a poor $\mathbf{k}\cdot\mathbf{p}$ description of band dispersion in *bulk* zinc-blende bands, and hence of the position of zinc-blende states which mix in the heterostructure due to zone folding. Although applied to the $(AlAs)_5(GaAs)_5$ superlattice, our explanations provide a general framework for understanding the weaknesses of the $\mathbf{k}\cdot\mathbf{p}$+EFA approach.

TABLE III. $(GaAs)_5(AlAs)_5$ superlattice (SL) near-edge states at $\overline{\Gamma}$ resolved into net contributions P_s [Eq. (14)] from bulk zinc-blende GaAs bands. Deviation from 1 of P (=sum of row entries) measures the extent to which the five spin-split zinc-blende bands retained adequately represent the SL state.

SL state at $\overline{\Gamma}$	GaAs band					Sum P
	CB2	CB1	hh	lh	*s-o*	
$\overline{\Gamma}(\Gamma_{6c})$	0.053	0.943	0	0	0	0.996
$\overline{\Gamma}(X_z)$	0.007	0.990	0	0	0	0.997
hh1	0	0	0.998	0.002	0	1.000
lh1	0	0	0.001	0.982	0.009	0.992
*s-o*1	0	0	0.051	0.137	0.808	0.996
hh2-*a*	0	0	0.933	0.035	0.030	0.998
hh2-*b*	0	0	0.970	0.024	0.001	0.995
lh2-*a*	0	0	0.029	0.947	0.020	0.996
lh2-*b*	0	0	0.011	0.829	0.153	0.993

Zone-center superlattice states which are derived mostly from zinc-blende Γ ($\equiv G_0$) states we expect will be well described by the standard model, since $\mathbf{k}\cdot\mathbf{p}$ bands are fit there. These include the hh1, lh1, and *s-o*1 hole bands (although the last is poorly described by the SM in the quantum well geometry). Deeper hole bands (hh2, lh2a, etc.), however, are derived mostly (Table II) from $G_j \neq \Gamma$ zinc-blende states *outside* the quadratic region where the $\mathbf{k}\cdot\mathbf{p}$ fit is good (see Fig. 2) and will be poorly described (Fig. 2) by the SM for moderate n. Such bands will be found *too deep* in the valence band, as seen in Figs. 5,7–10, and 12. Because the quadratic region is *largest* for the GaAs heavy-hole band, however, the SM reproduces ABP results for the hh2 band quite well for $n \gtrsim 10$ in Fig. 5.

$\mathbf{k}\cdot\mathbf{p}$ curves in Fig. 2 for the first bulk GaAs conduction band are already 280 meV *higher* than their ABP counterparts by the point G_1. As a result, since contributions from $G_j \neq 0$ are important (Table II), standard model predictions for the $\overline{\Gamma}(\Gamma_{6c})$ heterostructure conduction bands *must* be too high, as observed in Figs. 5, and 7–12.

As the GaAs thickness in a heterostructure increases, those points along the zinc-blende GaAs Δ direction which fold to the heterostructure zone center $\overline{\Gamma}$ move closer to the zinc-blende Γ point, eventually well into the region where $\mathbf{k}\cdot\mathbf{p}$ adequately represents the zinc-blende band structure. At the same time, the number of such points increases, and eventually near-edge heterostructure bands at $\overline{\Gamma}$ will *all* be well described by the standard model, as seen, e.g., in Fig. 5 for large n.

Based on the observations above, we can trace the relatively poor behavior of the standard model for systems with thin GaAs regions to an *inadequate description of the dispersion of bands of the constituent zinc-blende compounds at the wave vectors relevant to zone folding*. As we saw in Sec. II, a quantitative description of the dispersion of a *single* band in the $\mathbf{k}_0$ representation [Eq. (7)] on which the $\mathbf{k}\cdot\mathbf{p}$ approach is based, depends on retaining a sufficiently *large* number of zone-center Bloch states. Recent empirical pseudopotential tests[18] show that $\gtrsim 30$ zone-center states (including spin) are sufficient to quantitatively reproduce the full zone dispersion of near-edge zinc-blende bands.

The eight-band $\mathbf{k}\cdot\mathbf{p}$ approach used above for zinc-blende materials thus correctly focuses attention on four spin-split *bands*, but does not retain enough zone-center *states* to adequately describe their dispersion for systems with GaAs regions $\lesssim 40$ Å thick, to the accuracy required by experimental spectroscopic resolution ($\lesssim 10$ meV).

VI. SUMMARY AND CONCLUSIONS

Recently developed empirical pseudopotentials permit a complete, accurate description of bulk zinc-blende semicon-

ductors. From such calculations for GaAs and AlAs we extracted the Luttinger parameters required for an 8×8 multiband $\mathbf{k}\cdot\mathbf{p}$+EFA description of $(AlAs)_n(GaAs)_n$ superlattices and $(GaAs)_n$/AlAs quantum wells. We directly contrasted predictions of an all band pseudopotential approach, which includes all bands and their dispersion throughout the zone and predicts wave functions with full Bloch symmetry, with predictions of an 8×8 multiband $\mathbf{k}\cdot\mathbf{p}$+EFA approach. We examined band energies, wave functions, and dispersion for both methods and surveyed the general weaknesses of the standard model $\mathbf{k}\cdot\mathbf{p}$+EFA description using the all band pseudopotential results as a gauge.

Our analysis shows that the standard model errors for heterostructure states primarily reflect $\mathbf{k}\cdot\mathbf{p}$ errors in the bulk constituents, weighted by the amount by which bulk states participate in the heterostructure state. This simple, general statement permits us to determine when the standard model can be expected to work well for heterostructures: (a) when heterostructure states are derived from bulk states *well* described by $\mathbf{k}\cdot\mathbf{p}$, i.e., from states near the zinc-blende Γ point; (b) when $\mathbf{k}\cdot\mathbf{p}$ errors in the bulk are *large* (e.g., for L or X points), but such states do not occur with significant amplitude in heterostructure states in the near-edge energy range of interest. Situation (a) is seen to occur for near-edge heavy- and light-hole superlattice states [Fig. 5(b)] deriving from bulk GaAs near-Γ states (well described for $ka/2\pi\lesssim0.2$ [Fig. 2(b)] by $\mathbf{k}\cdot\mathbf{p}$). Situation (b) occurs for heterostructures for which bulk X and L point conduction bands are well above the Γ point conduction-band minimum, e.g., InGaAsP/InP or InAs/GaAs systems and (type I) GaAs/AlGaAs systems. Our analysis also shows when $\mathbf{k}\cdot\mathbf{p}$ errors are expected to be large. Examples include $\langle111\rangle$-orientation superlattices of direct gap constituents with small zinc-blende L-Γ splittings. In such systems there is a significant mixing of zinc-blende L character into heterostructure zone-center states. Franceschetti *et al.* have recently shown,[46] for example, that the $\mathbf{k}\cdot\mathbf{p}$ model gives an incorrect dependence of the electron effective mass on the degree of $\langle111\rangle$ ordering in GaP/InP structures, due to the failure to describe Γ-L coupling. It is interesting to note that if one considers a quantum film *in vacuum* (i.e., not supported by a barrier material), effective mass approach errors are very large,[47] even near the valence-band maximum. Application of the standard model thus requires careful examination of the position of the consituent materials band edge states, the valence- and conduction-band offsets, and the orientation and thickness of the heterostructure.

ACKNOWLEDGMENTS

We thank David Gershoni for providing his eight-band $\mathbf{k}\cdot\mathbf{p}$+EFA computer code and for useful discussions about its use, Kurt Mäder and Ron Maurer for many useful suggestions, Alberto Franceschetti and Lin-Wang Wang, and Sverre Froyen for suggestions about heterostructure state projections and the conjugate gradient program. This work was supported by the Office of Energy Research, Materials Science Division, US Department of Energy Grant No. DE-AC36-83CH10093.

APPENDIX: EXTRACTING LUTTINGER PARAMETERS FROM BULK PSEUDOPOTENTIAL BAND STRUCTURE CALCULATIONS

This appendix describes how empirical pseudopotential[2] results for bulk GaAs and AlAs were fit to extract Luttinger parameters suitable for use in superlattice and quantum well calculations using the eight-band $\mathbf{k}\cdot\mathbf{p}$+EFA approach. Band parameters measured experimentally or extracted from all band pseudopotential (ABP) calculations for bulk GaAs and AlAs and Luttinger parameters are compared and the incompleteness of the Luttinger parametrization is discussed briefly.

Within the 8×8 Kane model commonly used to represent the bands of bulk III-V semiconductors, as parametrized by Gershoni *et al.*,[22] near-edge band effective masses are related to the Luttinger parameters as follows:

$$\left(\frac{m_{\rm el}}{m_0}\right)^{-1}=\alpha+\frac{E_P}{E_g}\frac{(E_g+\frac{2}{3}\Delta_0)}{(E_g+\Delta_0)}, \tag{A1a}$$

$$\left(\frac{m_{s-o}}{m_0}\right)^{-1}=\gamma_1-\frac{1}{3}\frac{E_P}{E_g}\frac{\Delta_0}{(E_g+\Delta_0)}, \tag{A1b}$$

$$\left(\frac{m_{\rm hh}[001]}{m_0}\right)^{-1}=\gamma_1-2\gamma_2, \tag{A1c}$$

$$\left(\frac{m_{\rm lh}[001]}{m_0}\right)^{-1}=\gamma_1+2\gamma_2, \tag{A1d}$$

$$\left(\frac{m_{\rm hh}[111]}{m_0}\right)^{-1}=\gamma_1-2\gamma_3, \tag{A1e}$$

$$\left(\frac{m_{\rm lh}[111]}{m_0}\right)^{-1}=\gamma_1+2\gamma_3. \tag{A1f}$$

In Eqs. (A1) the γ_i are Luttinger parameters, E_g is the energy gap between the highest valence band and lowest conduction band at Γ, Δ_0 is the spin-orbit splitting, and $E_p\equiv2m_0/\hbar^2P^2$ (with $P\equiv-i\hbar/m_0\langle s|p_x|x\rangle$) is the energy scale measuring the importance of the dipole matrix element coupling the valence-band maximum and the conduction-band minimum at Γ. Effective masses for nondegenerate states are isotropic at Γ.

Treating E_g and Δ_0 as experimentally known, Eqs. (A1) constitute six equations in the five unknowns γ_1, γ_2, γ_3, E_P, and α. We thus have both an overdetermined system and a simple check of the consistency of the description. This overdetermination of parameters is an illustration of how the Kane model, even in principle, cannot be exact; we return to this issue below.

To extract the parameters above, we carried out bulk empirical pseudopotential calculations (Sec. III B) for zinc-blende GaAs and AlAs, neglecting the small lattice parameter mismatch between them. The resulting bulk band energies at Γ established E_g and Δ_0. Effective masses were found via the expression $\Delta E\simeq\hbar^2/2m^*(\Delta k)^2$, where Δk and ΔE are the deviations from the band extremum in k space and in energy. Energy shifts were tabulated on a $\mathbf{k}$ grid of points about Γ with Cartesian components spaced apart by $\Delta k=0.012\,\pi/a$. With the spin-orbit interaction included, zinc-blende bands expanded about Γ may be nonparabolic.[7] [001] and [111] band effective masses at Γ were determined

TABLE IV. Band parameters for GaAs and AlAs used as input for $\mathbf{k}\cdot\mathbf{p}$ calculations: (i) as computed from bulk pseudopotential band structure calculations (ABP) including spin-orbit; (ii) extracted by Gershoni *et al.* (Ref. 22) from experiment; and (iii) as used by Ram-Mohan *et al.* (RYA) (Ref. 27); m_0 is the free-electron mass. For each set the corresponding parameters of Eqs. (A1) are also given.

Parameter	GaAs			AlAs		
	ABP	Gershoni	RYA	ABP	Gershoni	RYA
$E_g \equiv E_{\text{gap}}^{\text{dir}}$ (eV)	1.5288	1.519	1.521	3.0505	3.0995	3.031
Δ_0 (eV)	0.3411	0.341	0.34	0.314	0.300	0.275
$(\Delta V)_{\text{VBM}}$ (eV)	+0.500	+0.499	0.460	≡0.000	≡0.000	≡0.000
m_{el}/m_0	0.0831	0.0665	.0593	0.152	0.150	0.129
m_{hh}/m_0 [001]	0.386	0.340	0.377	0.457	0.478	0.478
m_{lh}/m_0 [001]	0.109	0.094	0.091	0.200	0.208	0.208
m_{hh}/m_0 [111]	0.948	0.816	0.952	1.087	1.149	1.149
m_{lh}/m_0 [111]	0.0952	0.0809	0.0791	0.161	0.166	0.166
$m_{s\text{-}o}/m_0$	0.208	0.178	0.172	0.309	0.312	0.294
γ_1	5.895	6.790	6.850	3.60	3.45	3.45
γ_2	1.652	1.924	2.10	0.70	0.68	0.68
γ_3	2.420	2.782	2.90	1.34	1.29	1.29
E_P (eV)	27.4	28.8	25.7	35.4	25.7	21.1
α	-4.79	-2.76	1.00	-4.68	-1.38	1.00

simply from the ΔE at the first grid point, since no terms linear in Δk were observed in our fits.

To compute band energies for heterostructures, we require one additional parameter, which is *not* a property of a pure material in isolation. This is the valence-band offset $(\Delta V)_{\text{VBM}}$ between the two materials (Table IV). The process of generating the pseudopotentials used in our calculations[2] naturally includes the *experimental* value for the valence-band offset. Table IV gives band parameters for GaAs and AlAs and the Luttinger parameters extracted by solving the first five of Eqs. (A1). Columns labeled[22,27] Gershoni, Henry, and Baraff (GHB) and Ram-Mohan, Yoo, and Aggarwal (RYA) give an indication of the variation in parameters used in $\mathbf{k}\cdot\mathbf{p}$+EFA calculations, although band effective masses, for example, are relatively insensitive[48] to Luttinger parameters. From our calculated values, we can examine some aspects of the consistency of the Luttinger description of bulk bands. In the [111] direction, for example, the light- and heavy-hole effective masses depend [Eq. (A1)] only on the Luttinger parameters γ_1 and γ_3, both of which are known from fitting five of the six equations above to the six (calculated) band effective masses. We will, for convenience, regard the equation for $m_{\text{lh}}[111]/m_0$ as a check on the presumed values of γ_1 and γ_3. We thus have an error in the [111] light-hole effective mass of

$$\frac{\Delta m_{\text{lh}}}{m_{\text{lh}}^{\text{ABP}}} = \begin{cases} -2.1\%, & \text{GaAs} \\ +0.16\%, & \text{AlAs.} \end{cases}$$

Thus the assumptions made in the 8×8 Kane model parametrization for bulk GaAs and AlAs are quite well obeyed by the ABP bands. The effect on band properties of the number N of states retained [Eq. (6) of the text] in the description has been examined by a number of authors.[19–21] One often finds large quantitative differences in the values of the Luttinger parameters obtained.

*Permanent address: Department of Physics, Colorado School of Mines, Golden, CO 80401; electronic address: dmwood@physics.mines.edu

[1] See, e.g., *Nanostructures and Quantum Effects*, Springer Series in Materials Science Vol. 31 (Springer-Verlag, Berlin, 1994).

[2] K. A. Mäder and A. Zunger, Phys. Rev. B **50**, 17 393 (1995), describe in detail the analytic form for the empirical pseudopotentials used in the present paper, how its parameters were fit to experimental data, and the tests applied.

[3] L.-W. Wang and A. Zunger, J. Phys. Chem. **98**, 2158 (1994); Phys. Rev. Lett. **73**, 1039 (1994); J. Chem. Phys. **100**, 2394 (1994).

[4] We assume that the system is periodic; use of a supercell geometry permits even isolated nanostructures, e.g., a quantum well, to be treated using the methodology and notation of an infinite crystal.

[5] See, M. C. Payne, M. P. Teter, D. C. Allan, T. A. Arias, and J. D. Joannopoulos, Rev. Mod. Phys. **64**, 1045 (1992).

[6] *Spectroscopy of Semiconductor Microstructures*, Vol. 206 of *NATO Advanced Study Institute, Series B: Physics*, edited by G. Fasol, A. Fasolino, and P. Lugli (Plenum, New York, 1989).

[7] E. O. Kane, in *Physics of III-V Compounds*, edited by R. K. Willardson and A. C. Beer, Semiconductors and Semimetals, Vol. I (Academic, New York, 1966), p. 75.

[8] E. O. Kane, in *Handbook on Semiconductors*, edited by T. S. Moss (North-Holland, Amsterdam, 1982), Vol. 1, Chap. 4A, pp. 193–217, presents a clear summary of the usual implementation of $\mathbf{k}\cdot\mathbf{p}$ theory.

[9] See, e.g., G. Bastard, J. A. Brum, and R. Ferreira, in *Solid State Physics: Advances in Research and Applications*, edited by D. Turnbull and H. Ehrenreich (Academic, New York, 1991), Vol. 44, p. 229.

[10] G. Bastard, C. Delalande, Y. Guldner, and P. Voisin, Adv. Elec-

tron. Electron Phys. **72**, 1 (1988).

[11] K. Ebertl, W. Wegscheider, and G. Abstreiter, Superlatt. Microstruct. **9**, 31 (1991).

[12] S. B. Zhang, C.-Y. Yeh, and A. Zunger, Phys. Rev. B **48**, 11 204 (1993).

[13] D. L. Smith and C. Mailhiot, Rev. Mod. Phys. **62**, 173 (1990), review tight-binding descriptions of semiconductor heterostructures. Section IV compares predictions of $\mathbf{k}\cdot\mathbf{p}+$ EFA with other theoretical methods.

[14] L. J. Sham and Y.-T. Lu, J. Lumin. **44**, 207 (1989).

[15] J. M. Luttinger and W. Kohn, Phys. Rev. **97**, 869 (1955).

[16] For a specified Hamiltonian, degenerate perturbation theory (DPT) differs from full diagonalization only in how the set of basis functions is chosen. In DPT *only* basis functions strongly coupled by the perturbation are retained; a complete set is not used. When the perturbation is strong enough to couple significantly to states *outside* the set, DPT fails or, in the general case, basis set incompleteness effects begin.

[17] States not explicitly included in the truncated set of zone-center states could be included by Löwdin perturbation theory. See the reviews of Kane (Refs. 7 and 8); C. Priester and M. Lannoo, Phys. Rev. B **44**, 10 559 (1991) discuss the effect of Löwdin perturbation theory on band nonparabolicity. The conventional Kane model (Refs. 7 and 8) includes parameters that for cubic systems acquire nonzero values *only* through couplings to states outside the eight retained. Elements of the matrix in Eq. (7) are thus formally energy-dependent perturbation sums of momentum matrix elements. In practice, the fitting process circumvents this procedure, however.

[18] L.-W. Wang and A. Zunger (unpublished).

[19] P. P. von Allmen, Phys. Rev. B **46**, 15 382 (1992).

[20] A. T. Meney, B. Gonul, and E. P. O'Reilly, Phys. Rev. B **50**, 10 893 (1994), review approximations often made in the EFA and review other recent work.

[21] K. H. Yoo, L. R. Ram-Mohan, and D. F. Nelson, Phys. Rev B **39**, 12 808 (1989).

[22] D. Gershoni, C. H. Henry, and G. A. Baraff, IEEE J. Quantum Electron. **29**, 2433 (1993).

[23] See, e.g., J. P. Cuypers and W. van Haeringen, Phys. Rev. B **47**, 10 310 (1993); R. Eppenga, M. F. H. Schuurmans, and S. Colak, *ibid.* **36**, 1554 (1987); R. Winkler and U. Rössler, *ibid.* **48**, 8918 (1993).

[24] M. G. Burt, J. Phys. Condens. Matter **4**, 6651 (1992).

[25] G. A. Baraff and D. Gershoni, Phys. Rev. B **43**, 4011 (1991).

[26] Burt (Ref. 24) has shown that this assumption need not be restrictive, but, in practice, the incompleteness of, e.g., an 8×8 $\mathbf{k}\cdot\mathbf{p}$ description suggests this to be a limitation.

[27] L. R. Ram-Mohan, K. H. Yoo, and R. L. Aggarwal, Phys. Rev. B **38**, 6151 (1988); see their Table I.

[28] W. Nakwaski, Physica B **210**, 1 (1995) (to be published) gives recommended values for electrons and heavy holes for GaAs and AlAs.

[29] J. P. Cuypers and W. van Haeringen, Physica B **168**, 58 (1991).

[30] S.-H. Wei and A. Zunger, J. Appl. Phys. **63**, 5794 (1988) give the mapping of zinc-blende Brillouin zone points to those of a tetragonal superlattice and the classification by symmetry for odd and even n.

[31] The n_c value for the superlattice type II/type I transition is somewhat shifted, with respect to calculations (Ref. 32) not including the spin-orbit interaction, but otherwise identical to our own, which found $n_c\simeq9$. A smaller GaAs electron effective mass at Γ would shift n_c to larger values.

[32] K. A. Mäder and A. Zunger, Europhys. Lett. **31**, 107 (1995).

[33] W. Ge, W. D. Schmidt, and M. D. Sturge, J. Lumin. **59**, 163 (1994).

[34] Planar-averaged square moduli of Bloch states for [001] $(\mathrm{AlAs})_n(\mathrm{GaAs})_n$ superlattice have inversion symmetry about a plane containing anions (cations) for even (odd) n, so that peaks generally correspond to anion planes.

[35] Large enough values of the Kane parameter B' (taken zero in these calculations) can strongly lift the spin degeneracy away from $\overline{\Gamma}$. A value which reproduces the splitting of the hh1 state at a particular value of $q_\perp$, however, overestimates the lh1 splitting and severely underestimates the s-$o1$ splitting, the most prominent in the ABP bands.

[36] K. Mäder, Dissertation ETH (Eidgenössischen Technischen Hochschule), Zürich, 1992.

[37] P. Boring and B. Gil (unpublished), cited in Ref. 36.

[38] Some of these bands are artifacts of the superlattice geometry, with wave functions with the nodal structure of electrons (weakly perturbed by the GaAs/AlAs potential difference) in a box the length of the primitive cell used to simulate the quantum well.

[39] R. G. Dandrea and A. Zunger, Phys. Rev. B **43**, 8962 (1991), Sec. III.

[40] The GaAs third and fourth conduction bands (Fig. 2) make only very small contributions to superlattice conduction-band projections, and are thus omitted in our projections.

[41] Superlattice states at $\overline{\Gamma}$ are spin doublets; both members have identical projections to the precision specified in the tables. In order to establish the ''parentage'' of superlattice valence states, we must project them onto zinc-blende Bloch states of definite character with respect to the labels light hole, heavy hole, etc. Because heavy- and light-hole states are degenerate at the Γ point for zinc-blende materials, the numerical zinc-blende valence-band maximum is *a priori* an arbitrary admixture of light- and heavy-hole character. One could, in principle, project (Ref. 42) zone center Bloch states onto states of definite *total* angular momentum J to permit the classification above. Instead, to lift this degeneracy, numerical zinc-blende Bloch states nominally for Γ were actually evaluated at $k=2\pi/a(0,0,0.01)$, numerically shifted back to $2\pi/a(0,0,0)$, and then used for projections.

[42] Reference 7, Sec. 3(b) displays the states $|J,m_J\rangle$ at Γ for zinc-blende compounds. See also R. Eppenga, M. F. H. Schuurmans, and S. Colak, Phys. Rev. B **36**, 1554 (1987).

[43] G. Bastard, *Wave Mechanics Applied to Semiconductor Heterostructures* (Les Editions de Physique, Paris, 1988).

[44] H. Schneider, H. T. Grahn, K. von Klitzing, and K. Ploog, Phys. Rev. B **40**, 10 040 (1989).

[45] G. Edwards and J. C. Inkson, Semicond. Sci. Technol. **9**, 310 (1994).

[46] A. Franceschetti, S.-H. Wei, and A. Zunger, Phys. Rev. B **52**, 13 992 (1995).

[47] S. B. Zhang, C. Y. Yeh, and A. Zunger, Phys. Rev. B **48**, 11 204 (1993); Superlatt. Microstruct. **14**, 141 (1994). See, also, S. B. Zhang and A. Zunger, Appl. Phys. Lett. **63**, 1399 (1993).

[48] W. Hackenberg, R. T. Phillips, and H. P. Hughes, Phys. Rev. B **50**, 10 598 (1994).